Case Studies in Thermal Engineering 73 (2025) 106630

Contents lists available at ScienceDirect

Case Studies in Thermal Engineering

journal homepage: www.elsevier.com/locate/csite

Experimental observations and modelling of the downward longwave radiation in the Mediterranean region

Giovanni Arcidiacono [a,b], Stefano Aneli [a], Giuseppe Marco Tina [a], Antonio Gagliano [a,*]

[a] Department of Electrical, Electronic and Computer Engineering, University of Catania, Catania, 95125, Italy
[b] Department of Information and Electrical Engineering and Applied Mathematics, University of Salerno, Fisciano, 84084, Italy

ARTICLE INFO

Keywords:
Downward longwave radiation
Pyrgeometers
Sky temperature
Numerical models

ABSTRACT

Evaluating long-wave radiation is a critical task for controlling surface energy budgets in various application fields. The long-wave radiation can be estimated using surface observations alone, such as direct measurements by pyrgeometers in weather stations, or through empirical models based on air temperature and humidity, which are usually measured in most weather stations. Adaptability is the main limitation of the literature's empirical models; indeed, these models yield mediocre accuracy when applied in locations other than the original development site, where they were assessed. To overcome these limitations, this study presents the results of experimental observations to evaluate the accuracy of literature models when used within the Mediterranean Area. The cloudy cover, which is one of the main difficult data to retrieve for calculating the long wave radiation, has been determined using data derived from satellite data or metar stations. The comparisons between observations and literature models have evidenced that only a few literature models allow to achieve accurate results both under clear and cloudy sky conditions. This research presents observations on long-wave radiation in Catania, an area where no previous surveys were available. The identification of the most truthful literature models represents useful information for a more accurate evaluation of the long-wave radiation in the Mediterranean Region.

1. Introduction

The net radiation (RN) is a component of the surface energy balance, defined through the surface radiative balance between the absorbed solar radiation and the upward and downward longwave radiation (Rld). The Rld results from atmospheric re-emission of H2O, CO2, O3 molecules, and cloud droplets in the atmosphere near the Earth's surface. It is the reversible consequence of the absorption by the gases in the atmosphere of the longwave radiation emitted from the Earth [1]. Estimating the downward longwave radiation on the surface is essential for understanding the impact of increasing CO2 and other greenhouse gases (GHG) for studying changes in the Earth's climate [2,3]. While it is also the radiative component most poorly quantified from direct observations [4]. Estimating Rld is a critical task in controlling surface energy budget and subsequently renders a clue to yield accurate evapotranspiration (ET) estimations for many application fields, such as weather predictions and global climate change [5,6]. Rld can be determined from sophisticated radiative transfer models in the atmosphere (e.g. LOWTRAN [7], MODTRAN [8], or STREAMER [9]) to

* Corresponding author.
E-mail address: antonio.gagliano@unict.it (A. Gagliano).

https://doi.org/10.1016/j.csite.2025.106630
Received 21 March 2025; Received in revised form 15 June 2025; Accepted 3 July 2025
Available online 4 July 2025

simple empirical formulations. These radiative models require temperature and humidity profiles, cloud properties, and aerosols, usually unavailable at the sites where Rld should be evaluated, the lack of this data limits their practical usage. The usage of global reanalysis products provide, which estimates the lower atmosphere's temperature and humidity profiles, are accurate enough for the calculation of global Rld with a radiation transfer model. In recent decades, reasonably successful techniques have been developed to estimate Rld based on surface observations alone. Indeed, since under clear sky conditions the temperature and humidity of the lowest 100 m of the atmosphere above all determine Rld [10], simple physical or empirical models using air temperature and humidity, usually measured in most weather stations, have proved reliable [11,12].

In 1932, Brunt developed the first empirical relationship between R_{ld} and the square root of near-surface vapour pressure, "e" [13]. In 1963 Swinbank [14] and Idso & Jackson in 1969 [15], correlated R_{ld} to the square of the temperature [14]. The former estimated an RMSE of less than 5 W m^{-2}, while the last correlation had a correlation coefficient of 0.99. A physically rigorous parameterization of atmospheric emissivity based on the assumptions of standard atmospheric lapse rates of temperature and vapour pressure was proposed by Brutsaert (1975) [16]. Recently, the Brunt (1932) [13] and Brutsaert (1975) [16] models were applied by Wang and Liang [17], to estimate global R_{ld} under all sky conditions, mainly in North American sites.

The direct measurements of R_{ld} using pyrgeometers are challenging due to the cost of the measurement instruments, the spatial coverage of R_{ld} observation sites is scarce and even absent. Globally, only a few weather stations have long-term measurements of R_{ld} [18].

Coordinated monitoring activities with pyrgeometers have been made within the Baseline Surface Radiation Network (BSRN), a project of the *World Climate Research Programme* (WCRP) [19], the Coordinated Energy and water-cycle Observations Project (CEOP) [20], and the FLUXNET project [21]. The monitoring activities carried out at the BSRN sites have provided long-term continuous measurements of R_{ld} for nearly 20 years.

Instantaneous R_{ld} has been estimated using the Moderate Resolution Imaging Spectroradiometer (MODIS) atmospheric products under clear sky conditions [22] at 17 sites. The R_{ld} estimated through eight meteorological parameterization methods exhibited (RMSE) values less than 35 W m^{-2}.

Even though empirical models have had varying degrees of success, their main problem seems to be their versatility; indeed, as the methods have been empirically developed at one location and with one set of instruments they do not fare well in other sites. Often, those developing new methods later show [23]. In summary, R_{ld} can be estimated from ground-based observations, empirical methods, reanalysis systems, and satellite retrievals.

Although several studies provide numerical models for the calculation of the downward longwave radiation, there is a lack of analyses regarding their validity in different sites concerning their original development. In particular, there are no studies that have investigated the effectiveness of literature models in the Mediterranean region, as well as the availability of experimental data concerning direct measurements of the downward longwave radiation.

In this study, the results of experimental measurements done in Catania (south Italy) are presented. In Section 2 models for clear and cloudy sky parameterisations are described, as well as instrumentation for direct measurements. The experimental surveys carried out for clear and cloudy sky conditions and the analyses of the results are illustrated in Section 3. Conclusions are given in Section 4.

2. Long-wave radiation and surface energy budget

The evaluation of long-wave radiation is critical for assessing the surface energy balance of any surface on Earth, as it is one of the components determining the surface energy budget.

The surface energy budget is defined by the interaction of the heat fluxes between the earth's surface and atmosphere, that is the latent heat flux (λE), the sensible heat flux (H), and the heat storage in the ground (G), whose sum allows to determine the Net-Radiation (R_N) as expressed in Eq. (1).

$$R_N = \lambda E + H + G \tag{1}$$

Moreover, the Net radiation is evaluated through the surface radiative balance between the absorbed shortwave solar radiation (R_{sd}), the upward longwave radiation (σT_s^4), and the downward longwave radiation (R_{ld}), as defined by Eq. (2) [24].

$$R_N = R_{sd}(1-\alpha) + \varepsilon_s\left(R_{ld} - \sigma T_s^4\right) \tag{2}$$

An interesting option to reduce the cooling load of building is the exploiting of the radiative cooling by longwave radiation emission toward the sky, which can improve building energy performance. Outer space is an ideal and natural source of cooling for any terrestrial surface, which allows the exploitation of Radiative Cooling, a passive method to cool a surface (e.g. building roofs and façade [25]) The temperature in outer space is approximately equal to 3 K but the temperature of the sky measured overhead is higher, as the water vapour in the atmosphere absorbs the infrared radiation emitted by the underlying ground.

The longwave net radiative energy flux between a surface (q_{rad}) and sky vault is calculated as a function of the sky temperature (Eq. (4)).

$$q_{rad} = \varepsilon_s \cdot \sigma \cdot F_{s-sky} \cdot \left(T_s^4 - T_{sky}^4\right) \tag{3}$$

The evaluation of sky temperature (T_{sky}) and emissivity is fundamental and needs to be properly accounted [26]. The standard ISO 13790 [27] provides simplified correlations for calculating the sky temperature (see Table 1).

However, the ISO 13790 correlations provide just a reference value of (T_{sky}), which may not be sufficiently detailed for assessing

Table 1
ISO 13790 Correlation for the calculation of the sky temperature.

Site	Correlation	
Temperate areas	$T_{sky} = T_a - 11$	(3)
Sub-polar areas	$T_{sky} = T_a - 9$	(4)
Tropical areas	$T_{sky} = T_a - 13$	(5)

the surface energy balance under variable weather conditions.

As general rule, the evaluation of R_{ld} is essential for assessing the energy balance under different weather conditions. Fig. 1 shows the different heat fluxes determining the energy balance for a building façade [28] and a solar panel [29] respectively. The energy balance for the solar panel can be expresses by Equation (4).

$$R_{ld} + R_{sd} + R_{lu,ground} = R_{ld,pan} + \alpha R_{sd} + R_{lu,pan} + H + E_{prod} \tag{4}$$

The similarity between the structure of solar panels and radiant coolers suggested that the integrated application of solar heating and radiative cooling can be addressed [30]. Gagliano et al. have developed an innovative system for exploiting nocturnal radiative trough solar panels.

In this patented study, the nocturnal radiative cooling is used for cooling the water flowing within the PV/T system, storing the cooled water in a tank and using it for reducing the cooling load of buildings, thus making a PV/T trigenerative plant [24].

The effects of the geometric structure, ambient temperature, and sky temperature on the radiative cooling power were analysed in Ref. [31].

3. Materials and methods

The downward longwave radiation results from atmospheric re-emission, due to the reversible effect of absorption of longwave radiation emitted from the earth by chemical elements in the atmosphere. Water vapour (H_2O), Oxygen (O_2), Ozone (O_3), and Carbon Dioxide (CO_2) are the main emitters of longwave radiation in the atmosphere in the range of 4.0–100.0 μm. R_{ld} can be determined by assuming black body behaviour or grey body behaviour at a uniform temperature, thus two alternative equations are defined:

$$\left\{ \begin{array}{c} R_{ld} = \sigma \cdot T_{sky}^4; \\ R_{ld} = \varepsilon_{atm} \cdot \sigma \cdot T_{atm}^4 \end{array} \right\} \tag{6}$$

It can be challenging to define the atmospheric emissivity (ε_{atm}) or the atmospheric temperature (T_{atm}) for a vertical column of the atmosphere. As a result, several models have been developed to estimate downward longwave radiation based on the ambient temperature (T_a) and/or the water vapour pressure (e_a) near the surface. If the ambient temperature (T_a) is used, the long-wave radiation can be expressed by Eq. 9

$$R_{\mathrm{ld}} = \varepsilon_{\mathrm{sky}} \sigma T_a^4 \tag{7}$$

The sky temperature is obtained by equating Eq. (8) and Eq. (9):

$$T_{\mathrm{sky}}^4 = \varepsilon_{\mathrm{sky}} T_a^4 \tag{8}$$

Thereby, for calculating the downward longwave radiation it necessary to find relations allowing to determine the sky emissivity

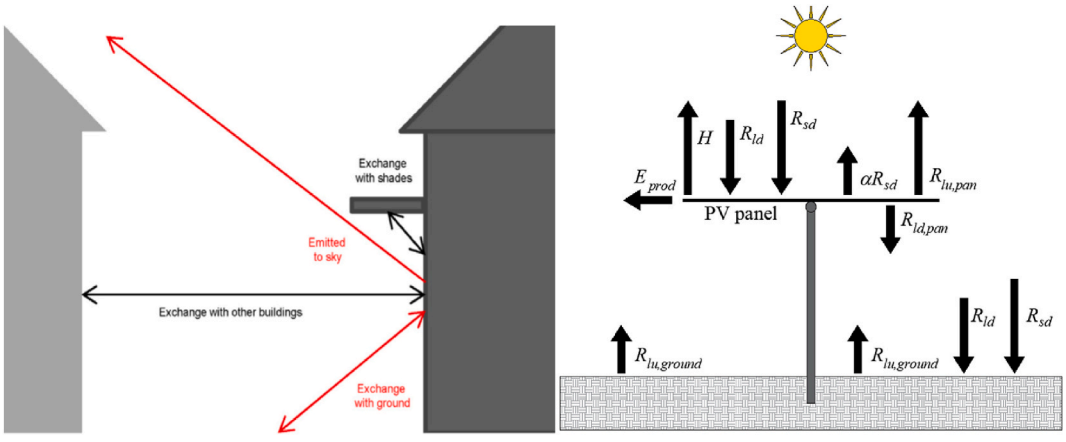

Fig. 1. Longwave radiation exchanges at the exterior surface of a building (a). Energy balance of a solar panel (b).

(ε_{sky}) as a function of water vapour pressure (e_a) and/or T_a, as shown in Eq. (11).

$$R_{ldc} = \varepsilon_{sky}(T_a, e_a)\sigma T_a^4 \tag{9}$$

To this aim, several empirical models based on least squares regression have been developed. Table 2 reports empirical formulations widely used in the literature for clear skies, which were developed using the atmospheric data observed in different regions.

The partial vapour pressure e_a [10^{-3} bar] is determined through Eq. (10), in which R_h is the relative humidity.

$$e_a = R_h\, exp[65.81 - 7066.2 / T_a - 5.976\, ln(T_a)] \tag{22}$$

The limit of the previous empirical models is to consider only clear sky conditions.

Since the sky emissivity is higher on cloudy days than on clear days, it was necessary to develop empirical models, which take into account the cloud cover. Typically, the cloudy-sky models are derived from clear skies models using the percentage of sky covered by clouds, namely cloud fraction cover (CFC).

Eqs. (25) and (26) [12,23] present two alternative methods used for calculating the long wave sky radiation under cloudy conditions (R_{ld}).

$$R_{ld} = R_{ldc}\left(1 + aCFC^{\,b}\right) \tag{23}$$

$$R_{ld} = R_{ldc}(1 - CFC^{\,c})\nu CFC^{\,c}\sigma T_a^{\,4} \tag{24}$$

Where a, b, c and ν are constant experimentally determined.

Table 3 shows some of the literature methods used to estimate R_{ld}, which include the cloud fractional cover. It is worth observing that such models can also predict R_{ld} under clear sky, posing CFC = 0.

It is also helpful to point out that none of those empirical models includes only the contribution of the water vapour and does not evaluate the contribution of the other greenhouse gases.

3.1. Cloud fraction cover

The cloud fraction cover can be directly assessed by observing the number of overcast sectors, assuming the whole sky subdivided into 10 sectors.

3.1.1. Satellite observation

As far as the cloud fraction is concerned, it is possible to obtain data on CFC from satellite-based earth observations. In this framework, the *Copernicus* project [34], which provides data for managing natural disasters, monitoring climate change, and studying the temporal evolution of the state of the oceans, vegetation, and atmosphere [1], can be used for deriving the CFC.

The available data are the results of a joint project between the European Agency for Satellite Meteorology (EUMETSAT) and the Satellite Application Facility on Climate Monitoring (CM SAF). In Copernicus, the CFC can be retrieved from the "*CLAAS-3 cloud data record based on SEVIRI observations*", which is publicly available via the CM SAF website [35]. The CLAAS-3 record provides cloud properties derived from inter-calibrated measurements of the SEVIRI sensor on board METEOSAT second-generation (MSG) satellites [36]. From this database, it is possible to obtain: the average daily cloud cover, the average diurnal cloud cover, or the average nocturnal cloud cover on a 0.05 x 0.05 grid (longitude x latitude). The *Panoply* software is used for data post-processing to achieve a graphical output.

Fig. 2 shows an image of the METEOSAT full disk, which includes Europe, Africa, and the Atlantic Ocean. It is possible to observe the spatial variation of the average daily CFC for September 27, 2023.

The fractional cloud cover for a site of interest can be determined by spatial interpolation between adjacent nodes [37].

Table 2
Empirical clear sky models.

Reference	Clear sky longwave radiation	
Brunt (1932) [6]	$R_{ldc} = (0.605 + 0.048e_a^{1/2})\sigma T_a^4$	(11)
Idso and Jackson (1969) [6]	$R_{ldc} = \{1-0.261\cdot\exp(-7.77\cdot10^{-4}(273-T_a)^2)\}\sigma T_a^4$	(12)
Brutsaert (1975) [6]	$R_{ldc} = 1.24(e_a/T_a)^{1/7}\sigma T_a^4$	(13)
Satterlund (1979) [6]	$R_{ldc} = \{1.08(1-\exp(-e_a(T_a/2016)))\}\sigma T_a^4$	(14)
Prata (1996) [6]	$R_{ldc} = \{1-(1 + 46.5(e_a/T_a))\cdot\exp((1.5 + 46.5\cdot3(e_a/T_a))^{1/2})\}\sigma T_a^4$	(15)
Anderson (1954) [23]	$R_{ldc} = (0.68 + 0.036e_a^{1/2})\sigma T_a^4$	(16)
Swinbank (1963) [23]	$R_{ldc} = (9.36\cdot10^{-6}T_a)\sigma T_a^4$	(17)
Idso (1981) [32]	$R_{ldc} = (0.7 + 5.95\cdot10^{-5}e_a\cdot\exp(1500/T_a))\sigma T_a^4$	(18)
Abramowitz (2012) [33]	$R_{ldc} = 0.031e_a + 2.84T_a - 522.5$	(19)
Angström (1924) [25]	$R_{ldc} = (0.83-0.18\cdot10(-0.067e_a))\sigma T_a^4$	(20)
Raman (1935) [25]	$R_{ldc} = (0.62 + 0.029e_a^{1/2})\sigma T_a^4$	(21)
Elsasser (1942) [25]	$R_{ldc} = (0.21 + 0.22\ln(e_a))\sigma T_a^4$	(22)

Table 3
Empirical models for all sky conditions.

Reference	All sky model	
Maykut and Church (1973) [6]	$R_{ld} = R_{ldc}(1 + 0.22\mathrm{CFC}^{2.75})$	(25)
Jacobs (1978) [6]	$R_{ld} = R_{ldc}(1 + 0.26\mathrm{CFC})$	(26)
Sugita and Brutsaer (1993) [6]	$R_{ld} = R_{ldc}(1 + 0.0496\mathrm{CFC}^{2.45})$	(27)
*Konzelmann*et al. (1994) [6]	$R_{ld} = R_{ldc}(1-CFC^{4})+0.952\mathrm{CFC}^{4}\ \sigma\ T_a^4$	(28)
Crawford and Duchon (1999) [6]	$R_{ld} = R_{ldc}(1-CFC) + CFC\ \sigma\ T_a^4$	(29)
*Duarte*et al., Eq. (21) (2006) [6]	$R_{ld} = R_{ldc}(1 + 0.242\mathrm{CFC}^{0.583})$	(30)
*Duarte*et al., Eq. (22) (2006) [6]	$R_{ld} = R_{ldc}(1-CFC^{0.671})+0.99\mathrm{CFC}^{0.671}\ \sigma\ T_a^4$	(31)

3.1.2. Surface observation

Cloud fractional cover data can also be derived from surface weather observations available through the Automated Surface Observing System (ASOS) [38]. ASOS' weather observations report several weather elements, among which the cloud sky conditions (i.e. cloud height and cloud taxonomy: clear, scattered, broken, overcast) up to 12,000 feet. The cloud taxonomy is differenced within three layers: namely low, medium, and high clouds. However, high clouds do not have a measurable effect on R_{ld} variability and/or additional effect at the earth's surface) [39].

ASOS network report is a text file, commonly named METAR (Meteorological Aerodrome Report), which is a codified message containing the weather conditions observed at a weather station. A METAR file, updated hourly or semi-hourly, classified the CFC into several groups as a function of the number of oktas where clouds are present, i.e. NSC, FEW = 1–2 oktas; SCT = 3–4 oktas; BKN = 5–7 oktas; and OVC = 8 oktas. The classification within each group is determined considering the highest value between the low and middle layers if the clouds are present in both. Table 4 reports a METAR "text-annotated" with the matching numerical interpretation adopted by the National Oceanic and Atmospheric Administration [40].

The weather station closest to the analyses carried out in this study is the Catania Fontanarossa weather station (ICAO code: LICC), whose data are publicly available for download from the Iowa State University of Science and Technology website [41].

3.2. Pyrgeometers measurements

A pyrgeometer measures the Rld from the difference between the downward longwave radiation from the atmosphere and the upward radiation from itself. Considering the thermopile sensor surface absorbs and emits as a blackbody and its voltage linearly related to the net gain of radiant power, the downward longwave radiation is determined by Eq. (34) [42].

$$R_{ld} = U_{emf}/S + \sigma \cdot T_b^4 \tag{32}$$

Where T_b is the measured temperature.

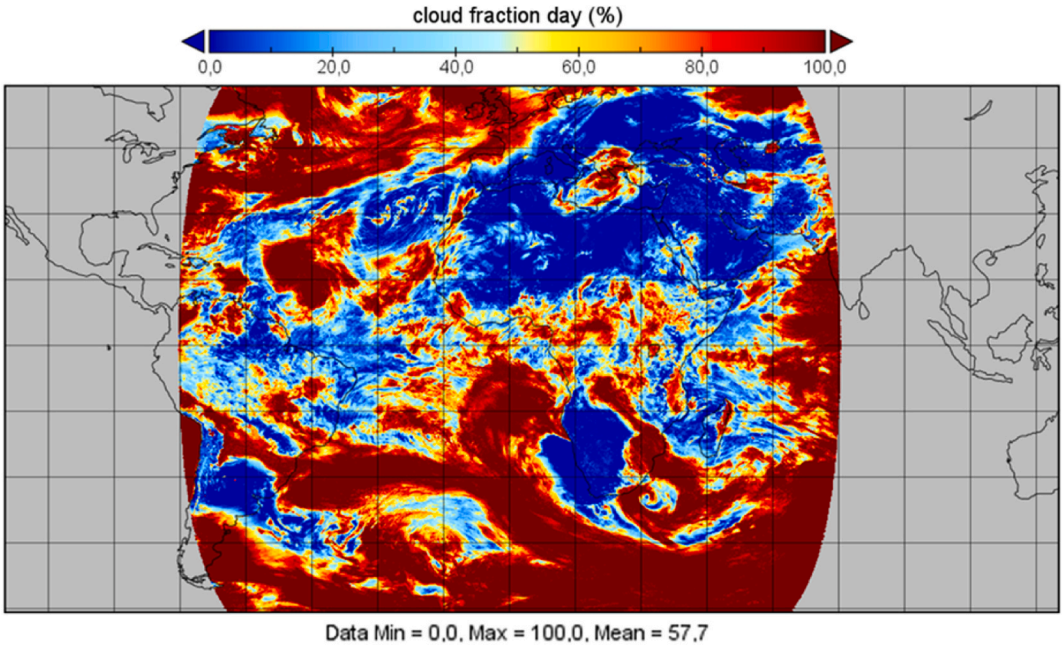

Fig. 2. Average diurnal daily CFC (2023, September 27) [34].

Table 4
METAR "text annotated" of cloud fraction.

METAR text-annotated cloud coverage	NSC	FEW	SCT	BKN	OVC
Numerical CFC	0	0.125	0.375	0.75	1

For a cloudy overcast sky, the upward radiation emitted by the earth is almost totally absorbed and re-emitted as downwelling radiation. As a result, the net radiation measured by the thermopile is a little negative (a few W/m^2), due to a small heat exchange between the relatively warm pyrgeometer and the colder sky. Under clear sky conditions, a relatively large heat loss occurs through the atmospheric window, resulting in a lower R_{ld} compared to overcast conditions. Conversely, during cloudy sky periods, the increased re-emission of downwelling radiation leads to a more pronounced negative net radiation, from −90 to −130 W m^{-2}.

Fig. 3 shows these two typical situations, in the left it is represented a cloudy sky conditions, when the downward radiation assumes a large value and consequently RN has low value, from 0 to −20 W m^{-2}, while in the right side is represented a clear sky conditions, when the downward radiation assumes small value and consequently RN has high value, from −90to −130 W m^{-2}), thus determining a meaningful cooling of the surface.

The main characteristics of the Kipp & Zonen CG3 pyrgeometer are shown in Table 5.

4. Experimental surveys

In this section, the empirical models exhibited in Tables 2 and 3, have been applied for calculating R_{ld}. The numerical results obtained are compared with experimental measurements conducted in Catania (37.52° N, 15.07° E) during September and October 2023. The analysis focuses on two clear-sky days and four cloudy-sky days. Meteorological data were recorded at 1-min intervals using an LSI data logger.

Figs. 4 and 5 show the Global Horizontal Irradiation (GHI), Direct Normal Irradiation (DNI), air temperature (Ta), and relative humidity (Rh) observed during two clear-sky days (September 27 and October 2) and two cloudy days (September 8 and 9), respectively.

4.1. Evaluation of R_{ld} beneath clear sky conditions

The Copernicus Climate Data classifies September 27 and October 2 as clear sky days (CFC-day = 0 %). Consequently, the hourly values of downward longwave radiation (R_{ld}) and sky temperatures were calculated using models suited for clear sky conditions.

Fig. 6 presents the predicted and observed data of R_{ldc}, as measured by the pyrgeometer on September 27 (left) and October 2 (right).

Fig. 7 displays the sky temperatures derived from Equation (10), using the observed values of R_{ldc}. during September 27 (left) and October 2 (right) ( ).

Each numerical model gives different predictions, some of which may be meaningful but inaccurate for the two investigated days (for example, Raman's model). In contrast, the clear sky model by Idso & Jackson provides R_{ld} predictions that align well with the observed data. Rld reaches its highest values during the central hours of the day, approximately 380 W m^{-2}, and its lowest values at night, around 350 W m^{-2}, which is consistent with atmospheric thermodynamics on a sunny day. The numerical data was more accurate on October 2, whereas some discrepancies appeared on September 27. Notably, the models failed to capture the peak value recorded by observations at 5:00 a.m., likely due to sparse clouds that the models did not detect. This issue will be investigated in the following sections. When comparing the models' results, significant variations in sky temperature (T_{sky}), from 270 to 287 K, are observed. The T_{sky} is consistently lower than the ambient air temperature (T_a) by 5–15 K and its diurnal distribution is like that of R_{ld}. Interestingly, the ISO standard for temperate climates provides only a constant difference of 11 K between T_{sky} and T_a. While the ISO norm provides a useful approximation of sky temperature, achieving higher accuracy requires the use of specific models or the availability of R_{ld} measurements. Calculations of T_{sky} using the Brunt, Angström, Raman, and Elsasser models show similar trends, but they differ by several degrees Kelvin. This discrepancy arises because these empirical models were developed based on local

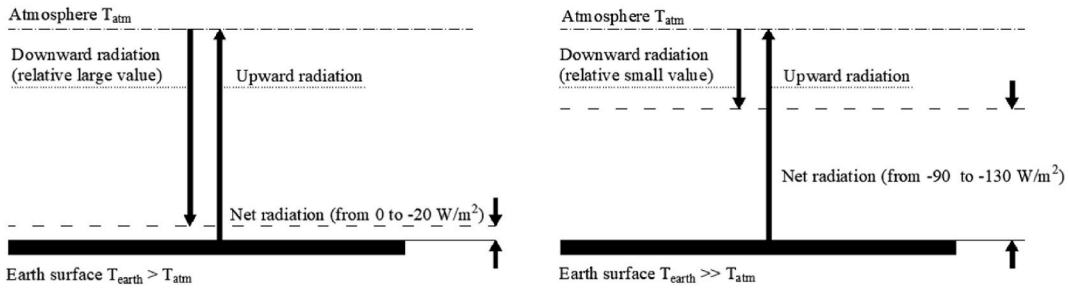

Fig. 3. Downward longwave radiation: a) Cloudy overcast sky; b) Clear sky conditions.

Table 5
Pyrgeometers main technical specifications (Kipp & Zonen CG3).

Performance	
Spectral range (50 % points)	4.5–42 μm
Sensitivity	5–15 μV/W/m^2
Response time	<18 s
Window heating offset	<15 W m^{-2}
Zero offset B	<4 W m^{-2}
Temperature dependence of sensitivity (−10 °C to +40 °C)	<5 %
Operational temperature range	−40 to +80 °C
Net irradiance range	−250 to +250 W m^{-2}
Field of view	150°
Non-linearity	<1 %

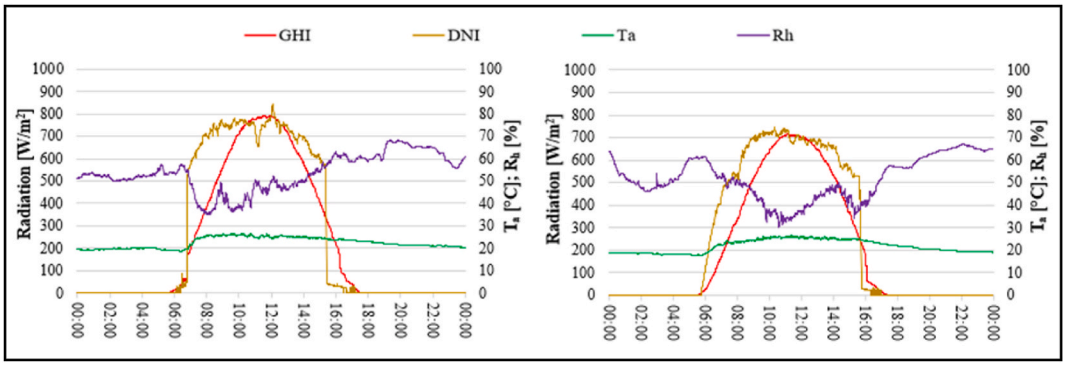

Fig. 4. Trends in weather variables on September 27 (left) and October 2 (right).

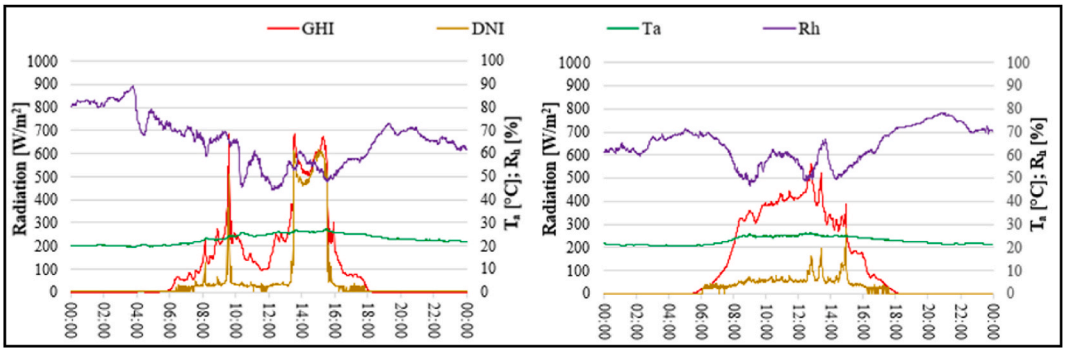

Fig. 5. Trends in weather variables on September 8 (left) and 9 (right).

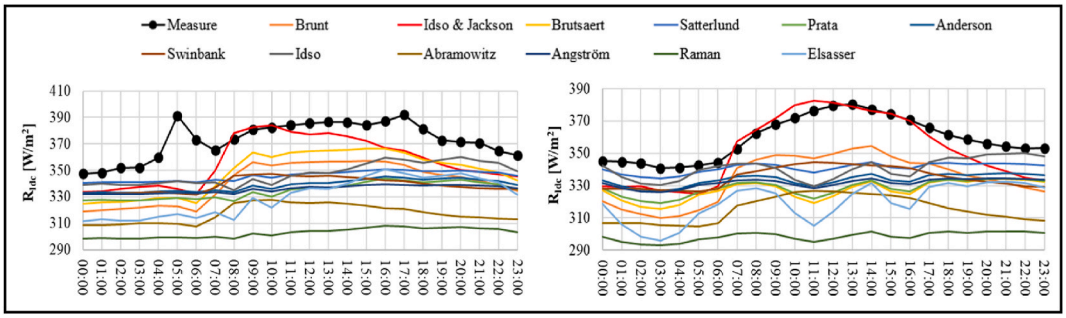

Fig. 6. Observed and calculated R_{ld} on September 27 (left) and October 2 (right).

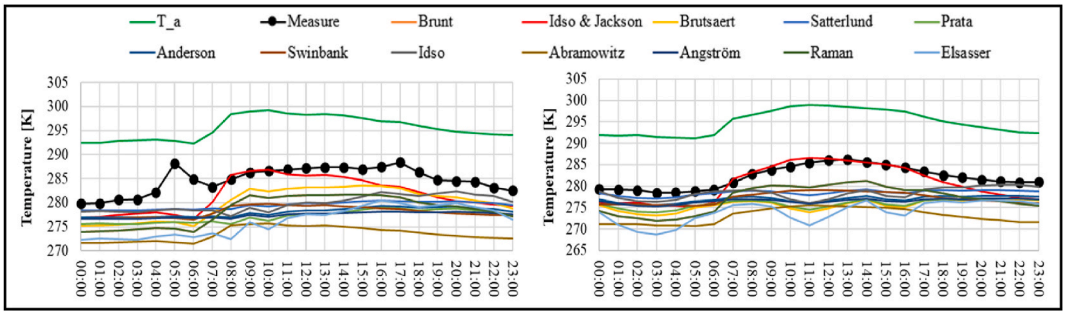

Fig. 7. Observed and predicted T_{sky} on September 27 (left) and October 2 (right).

atmospheric conditions in specific regions, such as Algeria, the United Kingdom, and India. As a result, they may not provide accurate predictions outside the areas where the models were initially tested. Table 6 shows the statistical analyses performed on September 27 to assess the accuracy of the investigated clear sky models.

Otherwise, the statistical analyses applied on Oct. 2 highlights better performance, assuming as reference the Idso and Jackson's model, the R^2 value decreases from −1.25 to 0.23 and MBE from 16.3 to 7.29 W m^{-2}.

On September 27, the limited accuracy of the models' forecasts was likely due to the presence of sparse low and middle clouds, as indicated by the METAR cloud coverage data. To account for these clouds, the downwelling longwave radiation was calculated.

Fig. 8 presents the value of R_{ld} calculated using the all-sky models on September 27.

Using cloudy sky models results in a significant improvement in the forecasts of nearly all models. It is clear that even a modest amount of cloud fraction (CFC) strongly influences the amount of downward longwave radiation (Rld). When the CFC is present (indicated by the grey dotted line), the observed Rld increases, reaching peak values close to 400 W m^{-2}. This finding confirms the consistency between the pyrogeometer observations and the CFC data derived from the METAR file. As anticipated, sparse clouds determine significant variations in the sky temperature. This result underscores the importance of accurately evaluating the CFC. The use of a clear sky model leads to an underestimation of more than 30 % (approximately 60 W m^{-2}) for R_{ld} and over 10 K for T_{sky}. However, the cloudy sky models give significant deviations in T_{sky}**.** from 272 to 293 K.

4.2. Evaluation of downward longwave radiation beneath cloudy sky conditions

Downward longwave radiation on cloudy sky days has been calculated using the empirical models presented in Table 2 and cloud cover derived from the e *CFC*-day Copernicus data.

The following days were taken as samples, September 25 and 26 with CFC-day of 33 and 64 %, September 8 and 9 with CFC-day of 90 and 100 %. The hourly value of the CFC provided by the METAR files for Catania Fontanarossa is used for the calculation. For September 8, 9, 25, and 26, Fig. 9 shows the hourly values of R_{ld} calculated through the empirical models for cloudy sky conditions, the CFC (grey dotted line) and the measured R_{ld} for September 8, 9, 25 and 26.

It can be observed that both the measured and modelled longwave radiation increase when CFC increases and vice versa. The discrepancy between the measurements and prediction could be attributed to the uncertainties in determining fractional cloud cover (CFC). It is worth to notice that the cloud cover at Fontanarossa's meteorological station (37.467, 15.05) could differ respect to the observation point (37.516, 15.006), located at the Catania's University campus.

Table 7 shows an example of the statistical analyses performed to evaluate the accuracy of the different models.

As a general finding, among the analysed models, Duarte's model (Equation (22)) is the most suitable for evaluating downward longwave radiation (Rld) under cloudy-sky conditions.

Fig. 10 illustrates the scatter plot obtained comparing the measured downward longwave radiation with the values of R_{ld} predicted by the Idso & Jackson model for clear sky conditions and Duarte's model (Equation (22)) for all-sky conditions.

From this scatter plot it is possible to derive the following linear regression equations, which is chtacterized by an R-squared value of 0.7421,

$$y = 0.9658x + 9.463 \tag{35}$$

Our global analyses have enabled us to identify the empirical literature model that best fits the experimental data. However, a significant limitation of this study is the restricted amount of experimental data available, which could enhance the proposed investigations further. In this context, could be of interest to investigate the numerical stability of the empirical models used for calculating the long-wave radiation [43–45].

4.3. Evaluation of net radiation

This section aims to show an example of calculation of Net Radiation during a clear sky day, as sample the September 12, 2023, has been selected. The evaluation of the Net Radiation (R_N) by Eq. (2), along with the assessment of R_{ld} also needs the knowledge of the

Table 6
Statistical analysis of clear sky models (September 27).

Model	R^2	MBE (W m^{-2})	RMSE (W m^{-2})	MAPE
Idso & Jackson	−1.25	16.3	20.6	0.046
Brutsaert	−2.7	24.5	26.5	0.066
Idso	−3.3	25.6	28.5	0.068
Satterlund	−3.7	27.4	29.8	0.072
Brunt	−5.0	32.2	33.5	0.086
Anderson	−6.0	34.3	36.3	0.091
Swinbank	−5.7	33.9	35.5	0.090
Angström	−7.2	37.3	39.2	0.099
Prata	−7.6	38.4	40.1	0.102
Elsasser	−9.7	43.0	44.8	0.115
Abramowitz	−16.0	55.7	56.6	0.149
Raman	−26.0	70.3	71.3	0.187

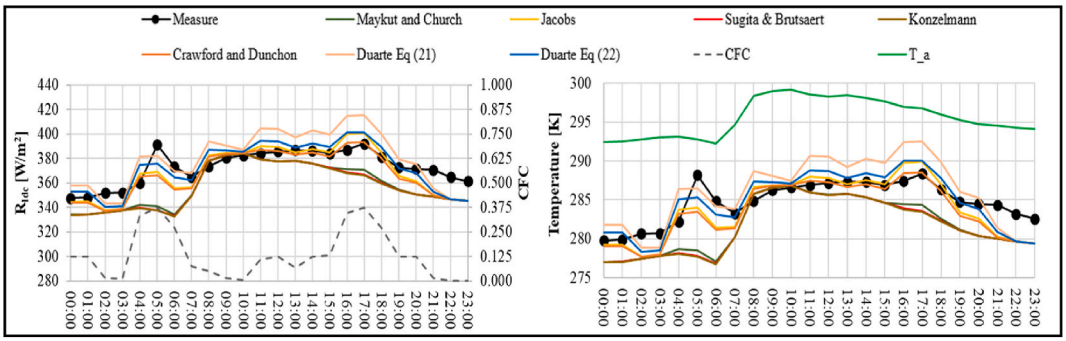

Fig. 8. All-sky model results and comparisons with measurements (September 27).

Fig. 9. All sky model results and comparisons with measurements (September 8, 9, 25, 26).

Table 7
All sky model statistical metrics at the Catania site (September 26, 2023).

Model	R^2	MBE (W m^{-2})	RMSE (W m^{-2})	MAPE
Maykut & Church	−0.907	32.2	38.6	0.084
Jacobs	0.150	13.0	25.8	0.049
Sugita & Brutsaert	−1.28	35.5	42.3	0.093
Konzelmann	−1.22	35.2	41.7	0.092
Crawford & Dunchon	0.157	15.7	25.7	0.048
Duarte Eq. 21	0.264	2.15	24.0	0.050
Duarte Eq. 22	0.353	8.34	22.5	0.043

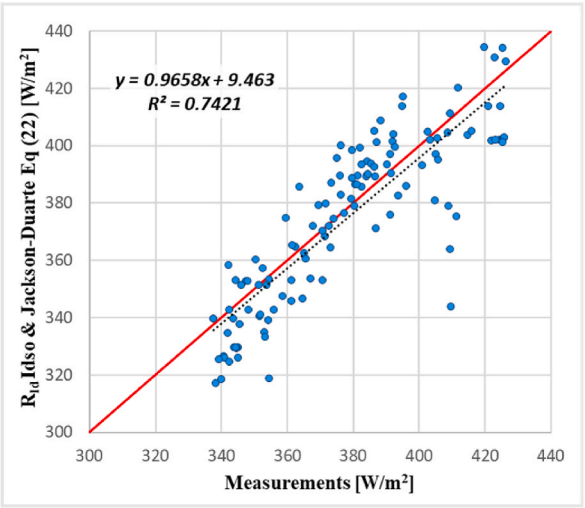

Fig. 10. Comparisons between the measured and modelled R_{ld} for all sky conditions.

Table 8
Clear sky net radiation (September 12–9:53 UTC). Note: "1" denotes values derived from measurements; "2" denotes values estimated with the Idso & Jackson model.

α	ε_s	T_S [K]	T_a [°C]	R_h [%]	R_{sd} [W/m^2]	$R_{ldc,1}$ [W/m^2]	$R_{ldc,2}$ [W/m^2]	$R_{N,1}$ [W/m^2]	$R_{N,2}$ [W/m^2]
0.206	0.971	314.87	28.42	40.00	661.00	382.37	371.26	379.34	365.41

short-wave albedo (α), surface emissivity (ε_S), and land surface temperature, (T_S), which can be derived from remote sensing analysis of Landsat 8 and 9 satellite imagery. The shortwave albedo was estimated using the Liang algorithm adapted to Landsat 8 and 9 spectral bands [46]:

$$0.356\rho_1 + 0.13\rho_3 + 0.373\rho_4 + 0.85\rho_5 + 0.072\rho_7 - 0.0018 \quad (33)$$

Where ρ_i represents the surface reflectance of the i-th band. Surface emissivity and land surface temperature were retrieved from Landsat 8–9 Level-2 Collection 2 products [47], with a spatial resolution of 100 m. Table 8 shows the comparison between the RN calculated on September 12 at 9:53 UTC using the observed and the R_{ld} calculated using the Idso & Jackson clear sky model.

Comparing $R_{N,1}$ and $R_{N,2}$, it can be observed that the net radiation estimated by the Idso & Jackson clear sky model differs by less than 4 % from that derived from measurements. This example highlights that starting from satellite data and observed/predicted data on R_{ld} allows us to determine R_N under given atmospheric conditions. It is worth mentioning that the knowledge of the Net Radiation is fundamental for the evaluation of the energy balance of any surface on the Earth, as well as for determining the evapotranspiration in green roof [48] or water basins [49].

5. Conclusions

This study illustrates the results of the experimental observations carried out through the pyrgeometer installed in the weather station of the DIEEI in Catania (south Italy), under clear and cloudy weather conditions. Subsequently, several literature models have been applied using as input data air temperature and relative humidity measured by the weather station installed at the same site. As regards the model used for the prediction of Rld under cloudy conditions, the fractional cloud cover has been derived from free online

available sources. In particular, the CFC data from Copernicus and METAR from Catania Fontanarossa have been used.

The comparisons between observations and measurements have evidenced that only a few literature models deliver quite accurate results for both clear and cloudy sky conditions. The truthfulness of these latter models is strictly related to the accuracy of the fractional cloud cover, which is the most difficult input to identify.

An imprecise assessment of the CFC of less than 1/8 oct, which could determine the use of a clear instead of cloudy model, gives rise to an underestimation of Rld of about 30 %.

However, the analyses carried out showed that the Idso & Jackson and Duarte models, for clear and cloudy conditions respectively, are those whose predictions are the more truthful for the investigated site. Moreover, the calculated/measured Rld has been used for the calculation of the Solar Net Radiation (RN), which is fundamental for determining the energy balance of the results of these preliminary surveys can be used as a reference as there are no previous surveys on Rld in the Sicilia Region.

Future development of this study aims to increase the experimental data to enhance the validation of the presented results and to create a new empirical model tailored to the investigated region.

CRediT authorship contribution statement

Giovanni Arcidiacono: Writing – review & editing, Writing – original draft, Visualization, Investigation, Data curation. **Stefano Aneli:** Validation, Resources, Formal analysis, Data curation. **Giuseppe Marco Tina:** Supervision, Resources, Formal analysis. **Antonio Gagliano:** Writing – review & editing, Supervision, Resources, Project administration, Methodology, Funding acquisition, Conceptualization.

Declaration of competing interest

The authors declare that they have no known competing financial interests or personal relationships that could have appeared to influence the work reported in this paper.

ACKNOWLEDGMENT

This study was funded by “PIAno di inCEntivi per la RIcerca di Ateneo 2024/2026" within the research project " Green Infrastructure and Renewable Energy for Sustainable Building Development”

The author Giovanni Arcidiacono acknowledges the Dottorato di Interesse Nazionale “Photovoltaics”

Data availability

Data will be made available on request.

References

[1] K. Wang, R.E. Dickinson, Global atmospheric downward longwave radiation at the surface from ground-based observations, satellite retrievals, and reanalyses, Rev. Geophys. 51 (2) (2013) 113–378.
[2] M.J. Iacono, J.S. Delamere, E.J. Mlawer, M.W. Shephard, S.A. Clough, W.D. Collins, Radiative forcing by long-lived greenhouse gases: calculations with the AER radiative transfer models, J. Geophys. Res. Atmos. 113 (D13103) (2008).
[3] G.L. Stephens, M. Wild, P.W. Stackhouse, T. L'Ecuyer, S. Kato, D.S. Henderson, The global character of the flux of downward longwave radiation, J. Clim. 25 (7) (2012) 2329–2340.
[4] K.E. Trenberth, J.T. Fasullo, Tracking earth's energy: from El Niño to global warming, Surv. Geophys. 33 (2012) 413–428.
[5] V. Sridhar, R.L. Elliott, On the development of a simple downwelling longwave radiation scheme, Agric. For. Meteorol. 112 (3–4) (2002) 237–243.
[6] M. Choi, J.M. Jacobs, W.P. Kustas, Assessment of clear and cloudy sky parameterizations for daily downwelling longwave radiation over different land surfaces in Florida, USA, Geophys. Res. Lett. 35 (L20402) (2008).
[7] F.X. Kneizys, E.P. Shettle, L.W. Abreu, J.H. Chetwynd, J.P. Anderson, W.O. Gallery, J.E.A. Selby, S.A. Clough, Users guide to LOWTRAN7, Environ. Res. Pap. (1988). Massachusetts.
[8] H.E. Snell, G.P. Anderson, J. Wang, J.-L. Moncet, J.H. Chetwynd, S.J. English, Validation of FASE (FASCODE for the environment) and MODTRAN3: updates and comparisons with clear-sky measurements, Proc. SPIE Conf. 2578 (1995) 194–204. Paris.
[9] J.R. Key, A.J. Schweiger, Tools for atmospheric radiative transfer: STREAMER and FLUXNET, Comput. Geosci. 24 (5) (1998) 443–451.
[10] J. Schmetz, Towards a surface radiation climatology: retrieval of downward irradiances from satellites, Atmos. Res. 23 (3–4) (1989) 287–321.
[11] J.H. Kjaersgaard, F.L. Plauborg, S. Hansen, Comparison of models for calculating daytime long-wave irradiance using long term data set, Agric. For. Meteorol. 143 (2007) 49–63.
[12] H.F. Duarte, N.L. Dias, S.R. Maggiotto, Assessing daytime downward longwave radiation estimates for clear and cloudy skies in Southern Brazil, Agric. For. Meteorol. 139 (3–4) (2006) 171–181.
[13] D. Brunt, Notes on radiation in the atmosphere, Q. J. R. Meteorol. Soc. 58 (247) (1932) 389–420.
[14] W.C. Swinbank, Long-wave radiation from clear skies, Q. J. R. Meteorol. Soc. 89 (381) (1963) 339–348.
[15] S.B. Idso, R.D. Jackson, Thermal radiation from the atmosphere, J. Geophys. Res. 74 (23) (1969) 5397–5403.
[16] W. Brutsaert, On a derivable formula for long-wave radiation from clear skies, Water Resour. Res. 11 (5) (1975) 742–744.
[17] K.C. Wang, S. Liang, Estimation of daytime net radiation from shortwave radiation measurements and meteorological observations, J. Appl. Meteorol. Climatol. 48 (3) (2009) 634–643.
[18] Y.Z. Wang, B. Jiang, S.L. Liang, D.D. Wang, T. He, Q. Wang, X. Zhao, J.L. Xu, Surface shortwave net radiation estimation from Landsat TM/ETM plus data using four machine learning algorithms, Remote Sens. 11 (23) (2019).
[19] A. Ohmura, E.G. Dutton, B. Forgan, C. Frohlich, H. Giglen, H. Hegner, A. Heimo, G. König-Langlo, B. McArthur, G. Müller, R. Philipona, R. Pinker, C. H. Whitlock, K. Dehne, M. Wild, Baseline surface radiation network (BSRN/WCRP): new precision radiometry for climate research, Bull. Am. Meteorol. Soc. 79 (10) (1998) 2115–2136.

[20] R. Lawford, M. Bosilovich, S. Eden, S. Benedict, C. Brown, A. Gruber, P. Hourser, K. Hsu, J. Huang, W. Lau, T. Meyers, K. Mitchell, C. Peters-Lidard, J. Roads, M. Rodell, S. Sorooshian, D. Tarpley, S. Williams, U.S. Contributions to the CEOP, Bull. Am. Meteorol. Soc. 87 (7) (2006) 927–939.
[21] D. Baldocchi, E. Falge, L. Gu, R. Olson, D. Hollinger, S. Running, P. Anthoni, C. Bernhofer, K. Davis, R. Evans, J. Fuentes, A. Goldstein, G. Katul, B. Law, X. Lee, Y. Malhi, T. Meyers, W. Munger, W. Oechel, K.T. Pau, K. Pilegaard, H.P. Schmid, R. Valentini, S. Verma, T. Versala, K. Wilson, S. Wofsy, FLUXNET: a new tool to study the temporal and spatial variability of ecosystem scale carbon dioxide, water vapor, and energy flux densities, Bull. Am. Meteorol. Soc. 82 (11) (2001) 2415–2434.
[22] H.R. Wu, X.T. Zhang, S.L. Liang, H. Yang, G.Q. Zhou, Estimation of clear-sky land surface longwave radiation from MODIS data products by merging multiple models, J. Geophys. Res. Atmos. 117 (D22) (2012).
[23] T.M. Crawford, C.E. Duchon, An improved parameterization for estimating effective atmospheric emissivity for use in calculating daytime downwelling longwave radiation, J. Appl. Meteorol. 38 (4) (1999) 474–480.
[24] V. Masson, M. Bonhomme, J.-L. Salagnac, X. Briottet, A. Lemonsu, Solar panels reduce both global warming and urban heat island, Front. Environ. Sci. 2 (2014).
[25] L. Evangelisti, C. Guattari, F. Asdrubali, On the sky temperature models and their influence on buildings energy performance: a critical review, Energy Build. 183 (2019) 607–625.
[26] International Organization for Standardization, ISO 13790: Energy Performance of Buildings - Calculation of Energy Use for Space Heating and Cooling, third ed., 2008. Geneva.
[27] V. Costanzo, G. Evola, A. Gagliano, L. Marletta, F. Nocera, Study on the application of cool paintings for the passive cooling of existing buildings in mediterranean climates, Adv. Mech. Eng. 5 (2013) 413675.
[28] Y. Zhang, R. Zhang, Y. Xiao, An improved radiative cooling flat-plate collector: numerical simulation and experimental study, Appl. Therm. Eng. 210 (2022).
[29] A. Gagliano, G. M. Tina, S. Aneli, High Efficiency Solar PVT Trigeneration System – Patent EP 4 056 922 A1.
[30] A. Chebihi, K.-H. Byun, J. Wen, T.F. Smith, Radiant cooling of an enclosure, Energy Convers. Manag. 47 (3) (2006) 229–252.
[31] R. Evins, V. Dorer, J. Carmeliet, Simulating external longwave radiation exchange for buildings, Energy Build. 75 (2014) 472–482.
[32] M. Li, Y. Jiang, C.F.M. Coimbra, On the determination of atmospheric longwave irradiance under all-sky conditions, Sol. Energy 144 (2017) 40–48.
[33] C. Sur, H. Kim, M. Choi, Satellite-based downward long wave radiation by various models in northeast Asia, Terr. Atmos. Ocean Sci. 25 (6) (2014) 893–902.
[34] https://www.copernicus.eu/en/about-copernicus.
[35] https://wui.cmsaf.eu/safira/action/viewProduktSearch.
[36] Product user manual ICDR AVHRR – based on CLARA-A2 methods cloud properties. https://www.cmsaf.eu/SharedDocs/Literatur/document/2021/saf_cm_dwd_icdr_clara_cld_pum_2_1_pdf.pdf?_blob=publicationFile&v=3, 2021.
[37] J.F. Meirink, R.A. Roebeling, P. Stammes, Inter-calibration of polar imager solar channels using SEVIRI, Atmos. Meas. Tech. 6 (9) (2013) 2495–2508.
[38] https://www.weather.gov/asos/.
[39] B. Dürr, R. Philipona, Automatic cloud amount detection by surface longwave downward radiation measurements, J. Geophys. Res. 109 (D5) (2004).
[40] National Oceanic and Atmospheric Administration, Automated surface observing system (ASOS) user's guide. https://www.weather.gov/media/asos/aum-toc.pdf, 1998.
[41] https://mesonet.agron.iastate.edu/request/download.phtml.
[42] R. Philipona, C. Fröhlich, K. Dehne, J. DeLuisi, J. Augustine, E. Dutton, D. Nelson, B. Forgan, P. Novotny, J. Hickey, S.P. Love, S. Bender, B. McArthur, A. Ohmura, J.H. Seymour, J.S. Foot, M. Shiobara, F.P.J. Valero, A.W. Strawa, The baseline surface radiation network pyrgeometer round-robin calibration experiment, J. Atmos. Ocean. Technol. 15 (3) (1998) 687–696.
[43] Z. Khan, W. Khan, Arko, A.S. Yagoub, R.H. Egami, H.A.L. Garalleh, Numerical stability of magnetized Williamson nanofluid over a stretching/shrinking sheet with velocity and thermal slips effect, Numer. Heat Tran., Part B: Fundamentals 86 (6) (2024) 1763–1783.
[44] Aisha M. Alqahtani, et al., Stability of magnetohydrodynamics free convective micropolar thermal liquid movement over an exponentially extended curved surface, Heliyon 9 (Issue 11) (2023) e21807.
[45] I. Khan Zeeshan, S.M. Eldin, et al., Two-dimensional nanofluid flow impinging on a porous stretching sheet with nonlinear thermal radiation and slip effect at the boundary enclosing energy perspective, Sci. Rep. 13 (2023) 5459.
[46] K. Naegeli, A. Damm, M. Huss, H. Wulf, M. Schaepman, M. Hoelzle, Cross-comparison of albedo products for glacier surfaces derived from airborne and satellite (Sentinel-2 and Landsat 8) optical data, Remote Sens. 9 (2) (2017) 110.
[47] https://www.usgs.gov/landsat-missions/landsat-collection-2-level-2-science-products.
[48] S. Cascone, J. Coma, A. Gagliano, G. Pérez, The evapotranspiration process in green roofs: a review, Build. Environ. 147, 337-355.
[49] F. Bontempo Scavo, G.M. Tina, A. Gagliano, S. Nižetić, An assessment study of evaporation rate models on a water basin with floating photovoltaic plants, Int. J. Energy Res. 45 (1), 167-188.

Nomenclature

R_{ld}: downward longwave radiation [W m^{-2}]
R_N: net radiation [W m^{-2}]
λE: latent heat flux [W m^{-2}]
H: sensible heat flux [W m^{-2}]
G: heat storage in the ground [W m^{-2}]
R_{sd}: downward shortwave radiation [W m^{-2}]
α: surface shortwave albedo [−]
ε_s: surface emissivity [−]
σ: Stefan-Boltzmann constant [W m^{-2} K^4]
T_s: surface temperature [K]
T_{sky}: sky temperature [K]
ε_{atm}: atmosphere emissivity [−]
T_{atm}: atmosphere temperature [K]
ε_{sky}: sky emissivity [−]
T_a: ambient temperature [K]
R_{ldc}: Clear sky downward longwave radiation [W m^{-2}]
e_a: water vapour pressure [10^{-3} bar]
R_h: relative humidity [−]
CFC: cloud fractional cover [−]
$R_{lu,ground}$: upward longwave radiation from the ground intercepted by the solar panel [W m^{-2}]
$R_{ld,pan}$: downward longwave radiation emitted by the solar panel to the ground [W m^{-2}]
$R_{lu,pan}$: long-wave radiation emitted and reflected by the solar panel to the sky [W m^{-2}]
E_{prod}: energy produced from the panel [W m^{-2}]
q_{rad}: net radiative heat exchange [W m^{-2}]
F_{s-sky}: sky-view factor [−]
U_{emf}: thermopile output voltage [μV]
S: pyrgeometer calibration factor [μV W^{-1} m^{2}]

T_b: body temperature [K]
n: number of observations (n = 24 since hourly averaged data are considered) [−]
y_i: hourly data observed [W m^{-2}]
$\widehat{y}_i$: hourly data estimated from empirical models [W m^{-2}]
$\overline{y}_i$: daily average data observed [W m^{-2}]
DHI: diffuse horizontal irradiance [W m^{-2}]
GHI: global horizontal irradiance [W m^{-2}]
ρ: Surface reflectance [−]